IOP Publishing Smart Materials and Structures
Smart Mater. Struct. **27** (2018) 125013 (15pp) https://doi.org/10.1088/1361-665X/aab575

Non-dimensional analysis of depth, orientation, and alignment in acoustic power transfer systems

David B Christensen and Shad Roundy

University of Utah, Salt Lake City, UT, United States of America

E-mail: david.christensen@dixie.edu

Received 21 July 2017, revised 20 February 2018
Accepted for publication 9 March 2018
Published 13 November 2018

Abstract

Acoustic power transfer systems are typically comprised of an electrical source, acoustic transmitter (TX), medium through which the acoustic waves propagate, acoustic receiver (RX) and an electrical load. The voltage generated across and power delivered to the load from the TX is a function of RX position (depth, orientation, and alignment relative to the TX), frequency, TX and RX diameter, and source and load impedance. In applications where the RX position is not fixed, such as in implantable medical devices, slight disturbances in RX position can result in a severe reduction in load voltage and power. Therefore, the sensitivity of voltage and power as a function of RX position is crucial to system design. This paper presents an analysis of the load voltage and power as a function of RX depth, orientation, alignment, frequency, RX and TX diameter, and load impedance. Design graphs are developed and presented as a means of visualizing the sensitivity of voltage and power to system parameters. Non-dimensional design graphs are then generated to broaden the applicability of simulation results.

Keywords: implantable devices, wireless power transfer, acoustic power transfer, ultrasonic transducers, acoustic wave propagation

(Some figures may appear in colour only in the online journal)

Introduction

Acoustic power transfer systems have gained interest in the past decade because of their application to implantable medical devices. Implantable medical devices are devices that are implanted into biological tissue to perform a diagnostic or therapeutic function. A recent review of acoustic power transfer for implantable medical devices can be found in [1]. Acoustic power transfer systems, as commonly defined in literature, are comprised of an electrical source, acoustic transmitter (TX), medium (e.g. tissue or water) through which acoustic waves propagate, acoustic receiver (RX), and electrical load. The electrical source powers the TX, which is typically piezoelectric. The TX is in contact with and emits acoustic waves into the medium to the RX which is implanted in the medium. The RX, which is typically piezoelectric, transduces the acoustic power into electrical power utilized by the electrical load (for example, a glucose sensor). For a fixed medium, the voltage generated across and power delivered to the electrical load are dependent on the following system parameters: load impedance, operating frequency, RX position relative to the TX, and TX and RX diameter. For transducers that have a circular cross-section, the RX position relative to the TX can be defined using three parameters: depth, angle, and offset. Depth is the axial distance between the TX and RX. Angle, also referred to as orientation, is the angle between the RX face and the TX face (i.e. angle is equal to zero when the TX and RX faces are parallel to each other). Offset, also referred to as alignment, is the lateral distance between the center of the TX and center of the RX. Depth, angle, and offset are defined graphically in figure 1.

The majority of published research papers addressing acoustic power transfer for implantable medical devices address, to some extent, voltage and/or power delivered to the load as a function of depth [2–25]. Papers addressing voltage and/or power delivered to the load as a function of offset and angle are fewer in number and can be found in [4, 5, 8, 11, 12, 15, 16, 21, 22, 26].

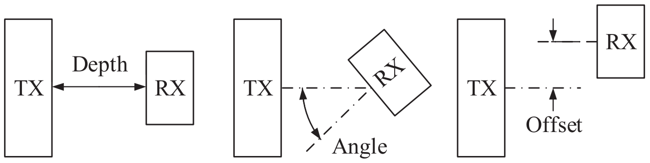

Figure 1. Diagram of depth, angle (orientation), and offset (alignment) degrees of freedom.

These papers consider orientation and alignment in a narrow scope: offering experimental and/or simulation data for a particular device. This information is useful for the particular device being analyzed, but offers limited insight into other acoustic power transfer systems. [12] provides dimensional simulation analysis on alignment and orientation using a finite difference time domain model for a specific device, but the analysis does not provide details about the effect that frequency, TX and RX diameter, and load impedance have on load voltage and power. To the authors' knowledge, an analysis of load voltage and power as a function of load impedance, operating frequency, depth, orientation, alignment, and TX and RX diameter specifically targeting acoustic power delivery has not been previously published.

Modeling techniques such as circuit equivalent models and 2D axisymmetric finite elements are unable to model the effects of orientation and alignment, but are commonly employed in literature because of their low computational cost. 3D finite element analysis has the capabilities to model the effects of orientation and alignment, but is rarely employed because of its high computational cost. Huygens principle, which discretizes the face of the TX into spherically radiating pressure sources, can be utilized to determine the power transferred to the RX for any position, orientation or transducer shape. However, this approach is not trivial to solve analytically for non-simple cases and does not account for pressure reflections between the TX and RX or the effect of electronics attached to the TX and RX. In order to efficiently model the effects of orientation and alignment while accounting for reflections and electronics, this paper employs a modeling technique that models the effect of depth, orientation, and alignment via ray tracing (DOART) as presented in [27]. DOART provides a reduction in computational cost that enables a more thorough exploration of the design and operational space of acoustic power transfer systems.

Of course, acoustic wave propagation and detection is a mature field with decades of theoretical development [28–30] Issues with signal propagation from and to cylindrical (i.e., piston shaped) transducers have been thoroughly studied in the context of sonar, radar, and medical imaging. Acoustic power delivery specifically for the purpose of providing electrical power to wireless electronic systems, such as biomedical implants, is an application of the general field of acoustics that has garnered considerable interest in the research community of late. While the underlying theory is the same whether the application is signal delivery (i.e., detection) or power delivery, there are specific considerations with power delivery that warrant investigation. For example, in the case of power delivery, operation is continuous, not pulsed, and narrowband. Additionally, the magnitude of the received voltage is more important for power delivery because of the need to directly rectify the voltage without amplification.

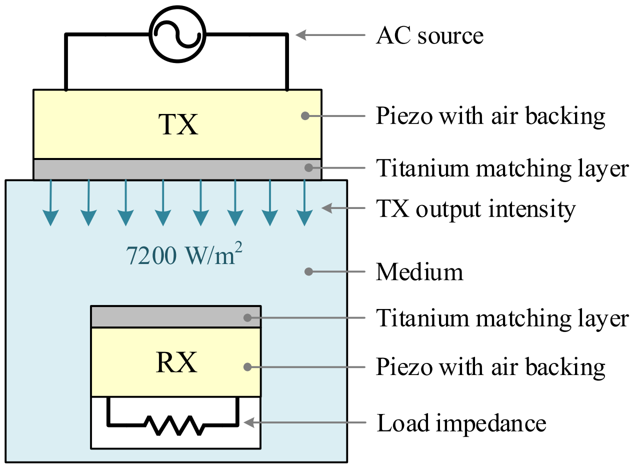

Figure 2. System diagram comprised of a source, TX, medium, RX, and load. The TX and RX have titanium matching layers and the TX emits an acoustic intensity of 7200 W m^{-2}.

The purpose of this paper is to provide an analysis of load voltage and power as a function of the system parameters previously mentioned. The analysis provides designers with a means of designing acoustic power transfer systems to be robust to power loss due to disturbances in depth, orientation, and alignment. In particular, the analysis can provide system designers with an estimate of operational uncertainty in voltage and power available for use. To accomplish this purpose, simulation data is analyzed dimensionally and compiled into design graphs to provide insight into voltage and power sensitivity to system parameters. Non-dimensional design graphs are then generated to broaden the applicability of the data. This paper presents the following: (1) modeling technique, system parameters and simulation assumptions. (2) Optimal load as a function of depth. (3) Voltage and power as a function of depth, and the depth magnitude and fluctuation design graphs. (4) Voltage and power as a function of angle, and the half angle design graph. (5) Voltage and power as a function of offset, and the half offset design graph. (6) Application of design graph data to scaled versions of the acoustic power transfer system using non-dimensional parameters.

System parameters and assumptions

A diagram of the acoustic power transfer system of interest is given in figure 2. The TX and RX are circular bulk-mode piezoelectric transducers with air backing and titanium matching layer. Matching layers are commonly built into acoustic transducers in order to increase the power emitted by the transmitter and transferred into the receiver. These layers tend to be a quarter wavelength thick with an acoustic impedance that is between the acoustic impedance of the piezoelectric material and the medium. Backing layers are typically employed to decrease the quality factor of the

Table 1. Material properties of the TX and RX piezo elements and titanium matching layer.

Material property	Units	Value
Piezo element		
Density	kg m^{-3}	7600
Speed of Sound	m s^{-1}	4025
Young's modulus (3-dir)	GPa	54
Relative permittivity	—	1950
Piezo coupling coeff. (3-3 dir)	—	0.46
Dielectric loss (loss tangent)	%	1.5
Mechanical quality factor	—	80
Titanium matching layer		
Density	kg m^{-3}	4500
Speed of sound	m s^{-1}	4916
Young's modulus	GPa	115

transducer and reduce ringing in the transmitted and received signals. For pulse-echo applications, both matching layers and backing layers are used to decrease the quality factor of the transducer for broadband operation. In power transfer applications, backing layers decrease the amount of power transduced. For this reason, air backing (or no backing layer) is assumed in this paper. Titanium is chosen as the matching layer because it is a bio-compatible material that is commonly used in medical applications. Material properties of the assumed piezoelectric material and titanium matching layer are given in table 1. To model this system efficiently, the DOART modeling technique as described in [27] is used to obtain simulation data. DOART approximates the behavior of the TX and RX using circuit equivalent models. Pressure propagation is simulated by discretizing the TX and RX and applying Huygens principle to propagate pressure rays from each element on the TX to each element on the RX. The Reflected Grid method, in conjunction with ray tracing, is used to account for the pressure ray reflections between the TX and RX. The resulting pressure on the RX face is fed into the RX circuit in order to calculate the load voltage and power. All simulation data assume that the TX and RX have the same resonance frequency and that the TX is operating at resonance. At resonance, the impedance of the TX and RX is typically a minimum. TX and RX impedance affects the reflection coefficient at the TX and RX face and thus affects the power that passes into the RX and the magnitude of reflections bouncing back and forth between the TX and RX. The TX outputs a continuous-wave acoustic intensity of 7200 W m^{-2}, which is the spatial-peak-temporal-average intensity limit in the human body for diagnostic ultrasound applications [31]. This intensity is used to provide an idea of achievable voltage and power levels in the dimensional graphs presented. The medium is considered to be homogeneous with an assigned absorption coefficient and absorption frequency exponent to account for absorption of acoustic waves through the medium. The apparent medium viscosity affects the quality factor of the transducer as described in [20]. Assumed material properties of the medium are meant to approximate lossy tissue, such as muscle, and are given in table 2 [20, 30].

Table 2. Material properties of the medium.

Medium properties	Units	Value
Density	kg m^{-3}	1070
Speed of sound	m s^{-1}	1566
Absorption coefficient	Np m^{-1} MHz^{-1}	15
Absorption freq. exponent	—	1
Kinematic viscosity	m^2 s^{-1}	0.15

Load

The first parameter of interest is the RX load because the optimal load resistance must be calculated (or an arbitrary load specified) before conducting further simulations. The optimal load in this paper is found by simulating the entire system to calculate load power as a function of real load impedance. Specifically, the power delivered to the load at a fixed depth for fifteen real impedance values between $1/10$ and $3/2$ times the magnitude of the impedance of the piezoelectric capacitance is calculated. Cubic spline interpolation is used between the fifteen points to create a more detailed power versus load curve (the error incurred using this approximation is found to be negligible). The optimal load impedance is chosen as the real impedance at which maximum power is delivered to the load. This procedure is repeated at ten evenly spaced depths over a half-wavelength depth range. Cubic spline interpolation is applied and the load impedance value is chosen as the mean. This impedance value is only recalculated when the frequency, TX diameter, or RX diameter changes. It is useful to note that although complex impedance matching increases load voltage and power, implant device size restrictions and associated achievable quality factor may render it impractical to include the required inductor in the device. With this assumption, the voltage and power levels in this paper represent a lower limit of theoretically achievable values. It is also useful to note that optimal load impedance changes with depth. This paper does not calculate the optimal load impedance at every depth, but rather assumes a fixed-average load impedance. The voltage and power penalty incurred by assuming a fixed-average load impedance is on the order of 1.43% and 0.03% for voltage and power respectively (for a 10 mm diameter TX and RX operating at 939.6 kHz between 5 and 50 mm depth). These figures are calculated as the magnitude of voltage or power at optimal load minus voltage or power at fixed-average optimal load divided by voltage or power at fixed-average optimal load

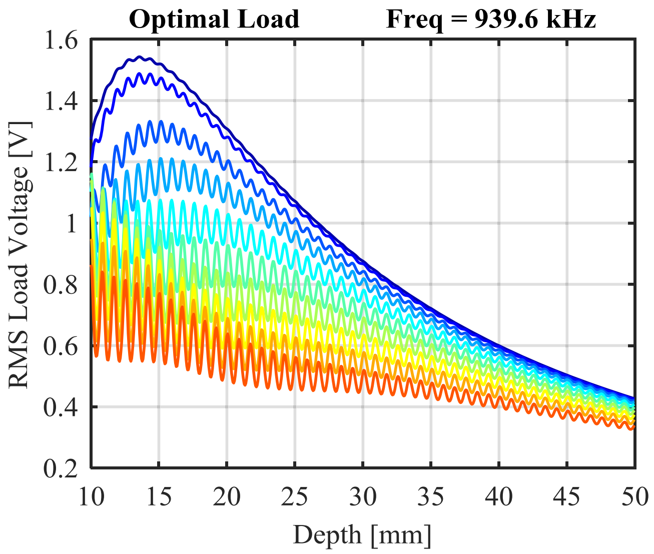

Figure 3. Load voltage as a function of depth for a 10 mm diameter TX operating at 939.6 kHz. This is the original simulation data before being split into mean (DC) and fluctuation (AC) components. Each line represents a RX diameter from 1 mm (dark blue) to 10 mm (red).

over the 5–50 mm depth range. For the remainder of this paper, all references to optimal load refer to the fixed-average optimal load, not the actual depth-dependent optimal load.

Depth

The second parameter of interest is depth. As the axial distance between the TX and RX changes, the load voltage and power fluctuate as a result of acoustic standing waves reflecting back and forth between the TX and RX. In graphical form, this data tends to look messy and is often difficult to compare with other similar data as shown in figure 3. Inspection of the data reveals that it can be interpreted as the superposition of two signals. The first signal is the large signal, or DC signal, that represents the mean value of the RMS voltage or average power as a function of depth. The second signal is the small signal, or AC signal, that represents the sinusoidal fluctuation in the RMS voltage or average power and is a result of standing waves. The distance between standing wave peaks, as seen by the load, is given in (1) where Δz is the change in depth required for the load voltage or power to encounter the next spatial resonance peak, c is the speed of sound in the medium, f is the operating frequency, and λ is the wavelength in the medium. Figure 4 gives a graphical example of how mean (DC) and fluctuation (AC) values of voltage are calculated. In the figure, voltage fluctuation is the difference between the peak and valley envelopes and the mean voltage is the mean of the peak and valley envelopes. It is important to emphasize that the voltage fluctuation can be seen as an uncertainty band because in actual operation it would not be possible to place or know the depth of an implant to the level necessary to ensure operation at a voltage peak. Furthermore, inhomogeneities in the medium will tend to diminish the

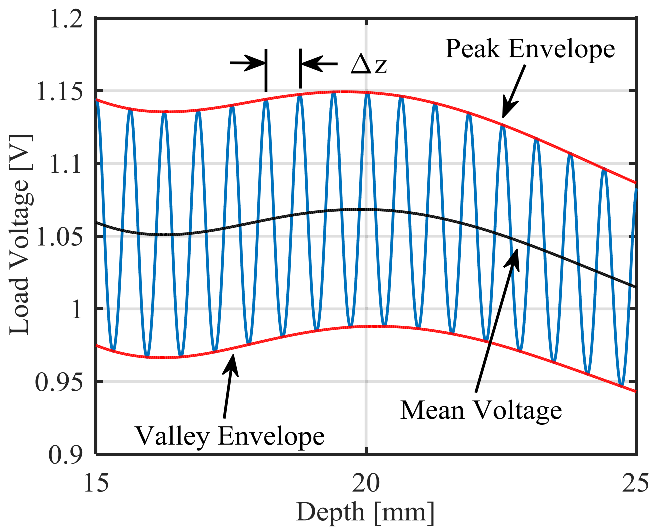

Figure 4. Decomposition of load voltage into a mean value and a fluctuation value. The fluctuation voltage is defined as the difference between the peak and valley envelopes. The mean voltage is defined as the mean of the peak and valley envelopes.

effect of the standing waves. Depth data is collected when angle and offset are equal to zero.

$$\Delta z = \frac{c}{2f} = \frac{\lambda}{2}. \tag{1}$$

The first design graph is the depth magnitude design graph and is demonstrated in figure 5. The depth magnitude design graph gives the mean voltage and power as a function of depth. In other words, it gives the DC signal of the depth data. It is useful to note that voltage is provided in addition to power as a practical reference as most power conditioning schemes will require a minimum voltage to operate. For example, the most common types of rectification are half-wave or full-wave rectifiers. The Schottky diodes employed in the rectifiers have a forward drop voltage of about 0.2–0.3 volts. This means that about 0.2–0.3 volts is lost across the diode for a half-wave rectifier. Full wave rectifiers have two forward drops, so the voltage lost doubles to 0.4–0.6 volts. After rectification, the DC voltage will likely need to be conditioned through a rectifier or DC–DC converter before being used by the load. This may require at least 0.2 volts DC post-rectification to operate. Each line in the depth magnitude design graph represents a RX diameter from 1 mm (dark blue) to 10 mm (red). The data show that voltage and power generally decrease with an increase in depth. This signal attenuation is a result of beam divergence and absorption in the medium. It is notable that the voltage is smaller for larger RX diameters, particularly near the Rayleigh distance. At the Rayleigh distance, 14.58 mm in this case, a maximum voltage is generated for smaller RX diameters. This is due to the nature of the acoustic beam emitted from the TX as shown in figure 6. An inspection of the figure reveals that the beam is more intense near the propagation axis and exhibits a high intensity region around the Rayleigh distance. The intensity profile in the figure is generated for a 10 mm diameter TX operating at 939.6 kHz using the analytical formulation described in [32] and evaluated using Gauss quadrature. It

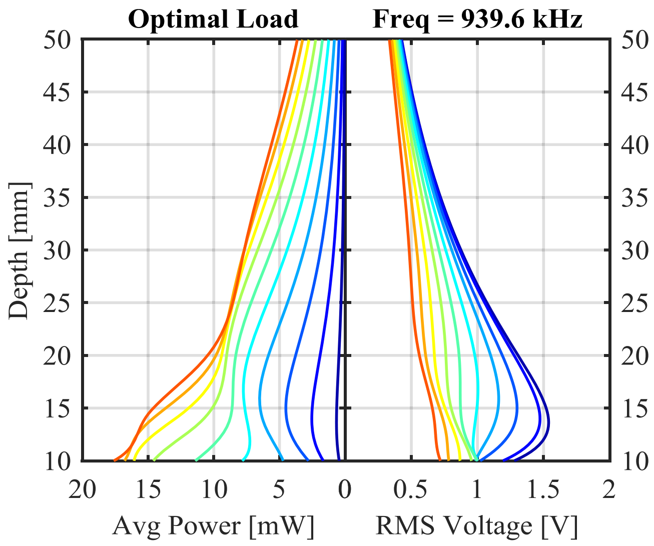

Figure 5. Depth magnitude design graph. Mean voltage and power as a function of depth for a TX and RX operating at 939.6 kHz with a fixed-average optimal load as described in the Load section of this paper. Each line represents a RX diameter from 1 mm (dark blue) to 10 mm (red).

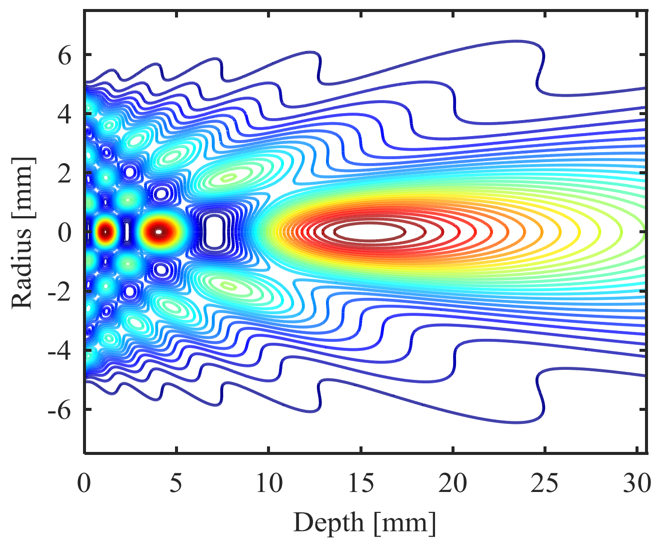

Figure 6. Contour plot of acoustic intensity emitted from a 10 mm diameter TX operating at 939.6 kHz. The radius axis indicates distance away from the center of the circular TX. Red indicates high intensity and blue indicates low intensity. Rayleigh distance is at 14.58 mm.

should be noted that simulation output from DOART exhibited an average 1.21% absolute error over 241 points when compared with the evaluation of the analytical formulation. A small RX placed in the high intensity region sees a high intensity on its entire face and generates a high voltage. A large RX placed in the high intensity region sees a high intensity at the center of its face and a low intensity on the edges of its face. This results in a lower average intensity on the RX face and thus a lower generated voltage. Also of note is that voltage and power for the 10 mm diameter RX (red line) continually increase with a decrease in depth. This is the case when depth is on the same order as or less than both the TX and RX diameters. Essentially, as the RX gets closer to the TX, less of the total beam power is able to escape around the sides of the RX. Larger diameter RXs are able to capture more of the total beam power and thus typically generate more power as shown in figure 5. Power scales proportionally to RX area for incoming plane waves because the intensity profile on the RX face is uniform. Power does not scale proportionally to RX area for realistic wave profiles, as shown in figure 6, because they do not produce a uniform intensity on the RX face.

The second design graph is the depth fluctuation design graph and is demonstrated in figure 7, The depth fluctuation design graph gives the voltage and power fluctuation that the load experiences when the RX depth changes by as little as $\Delta z/2$ to $3\Delta z/4$ and represents the AC signal of the depth data. Once again, each line represents a RX diameter from 1 mm (dark blue) to 10 mm (red). An example of how to read this graph is as follows: at 15 mm depth, the value of the red line (10 mm RX diameter) in the depth fluctuation voltage graph has a value of about 35%. In the depth magnitude voltage graph, the same red line at 15 mm depth has a value of about 0.65 V_{RMS}. This means that the greatest voltage fluctuation that the load will see is 35% of 0.65 V_{RMS} or 0.2275 V_{RMS}. According to (1), the distance between fluctuation peaks is 0.8333 mm. This means the RX would have to move between 0.4167 and 0.625 mm ($\Delta z/2$ to $3\Delta z/4$) in the depth direction to experience a 0.2275 V_{RMS} fluctuation. Again, as the precise location of the RX cannot usually be known or controlled to that level of precision, this graph can be interpreted as the uncertainty in voltage and power available to the implant. The data in figure 7 show that the magnitude of voltage and power fluctuation significantly increases for shallower depths and larger RX diameters. This is due to increased reflection activity that is able to occur between the TX and RX when the transducers are relatively close together.

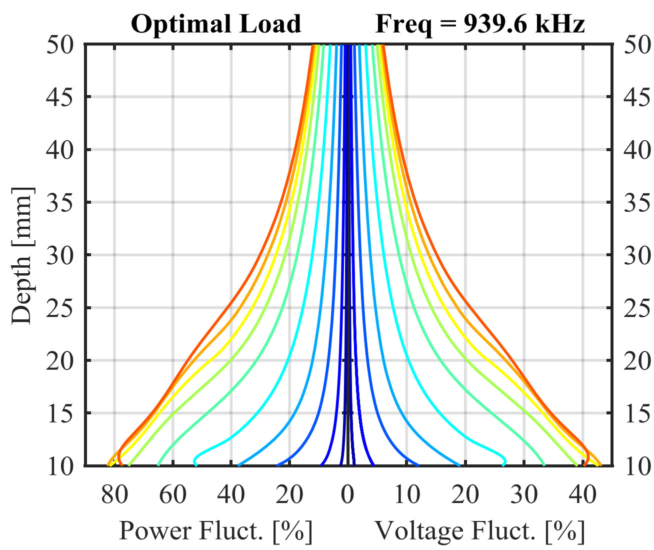

Figure 7. Depth fluctuation design graph. Voltage and power fluctuation percent as a function of depth for a TX and RX operating at 939.6 kHz and a fixed-average optimal load. Each line represents a RX diameter from 1 mm (dark blue) to 10 mm (red).

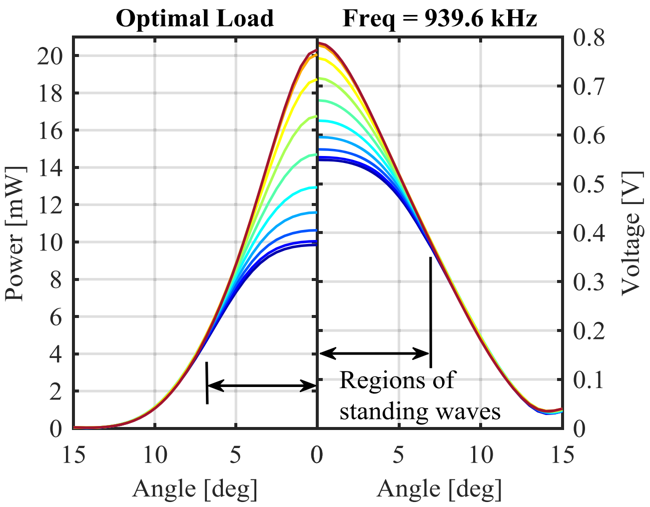

Figure 8. Voltage and power angle profile for a 10 mm diameter TX and RX operating at 939.6 kHz. Each line represents a fixed depth from 13.78 mm (dark blue) to 14.22 mm (red). The 13.78 mm line represents a valley and the 14.22 mm line represents a peak.

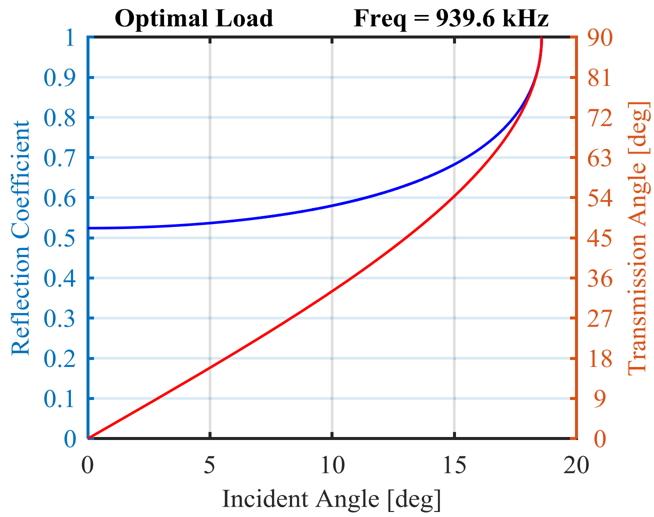

Figure 9. Reflection coefficient and transmission angle into the RX titanium matching layer of a single pressure ray as a function of incident angle for a 10 mm diameter RX operating at 939.6 kHz. Critical angle shown at 18.5°.

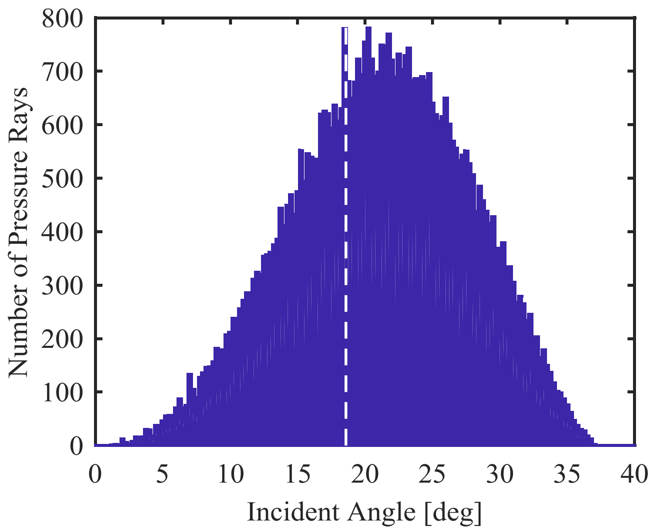

Figure 10. Histogram of pressure ray incident angles at the RX face for a 10 mm diameter TX and RX operating at 939.6 kHz and discretized with 226 elements each. The RX is positioned at 28.38 mm depth and oriented 20° relative to the TX. The critical angle of 18.5° is shown as the white dashed line.

Closeness in this case is defined as depth relative to the TX and RX diameter. For example, a 10 mm diameter TX and RX separated by a depth of 10 mm both appear to be one diameter away from each other. If the RX diameter were 5 mm, the RX would then appear to be two diameters away and thus apparently farther away than the 10 mm diameter RX. When considering this condition in terms of ray tracing, closer means that it is more difficult for pressure rays to stray. It should also be noted that if the RX were perfectly acoustically matched to the medium, no reflection activity would occur and thus voltage and power fluctuation would be zero.

Angle

The third parameter of interest is angle. As the angle between the TX and RX faces increases, three changes occur: (1) the reflection activity between the TX and RX decreases, (2) the effective reflection coefficient at the RX face increases, and (3) the pressure profile on the RX face changes. All of these changes contribute to a decrease in load voltage and power. To visualize the combined effect of these changes, an angle profile is created by measuring load voltage and power as angle is varied for a fixed depth and zero offset. Figure 8 gives voltage and power angle profiles for depths between a valley (at 13.78 mm depth) and a peak (at 14.22 mm depth) for a 10 mm diameter TX and RX operating at 939.6 kHz. Peaks and valleys are defined as the depths at which local maxima (peaks) and minima (valleys) in voltage or power are observed when depth is varied and the TX and RX are perfectly aligned and oriented (i.e. the local maxima and minima in figure 3). The graph shows that as angle increases, both voltage and power decrease. Change 1, a decrease in reflection activity, is easily noted by observing that the peak and valley lines have very different values at 0°. Between 0° and 7°, acoustic standing waves form between the TX and RX to create the peaks and valleys discussed in the Depth section of this paper. At around 7°, acoustic standing waves are unable to form, so the peaks and valleys completely disappear. Change 2, a decrease in reflection coefficient, is described by considering the analytical relation given in (2) where R is the reflection coefficient, θ_i is the incident angle at which a pressure ray strikes the RX, θ_t is the transmitted angle of the pressure ray into the titanium matching layer, Z_{RX} is the acoustic impedance of the RX with attached load, and Z_m is the acoustic impedance of the medium which is the density times the speed of sound. Figure 9 illustrates the reflection coefficient and transmitted angle for a single pressure ray striking a 10 mm diameter RX at 939.6 kHz. The RX acoustic

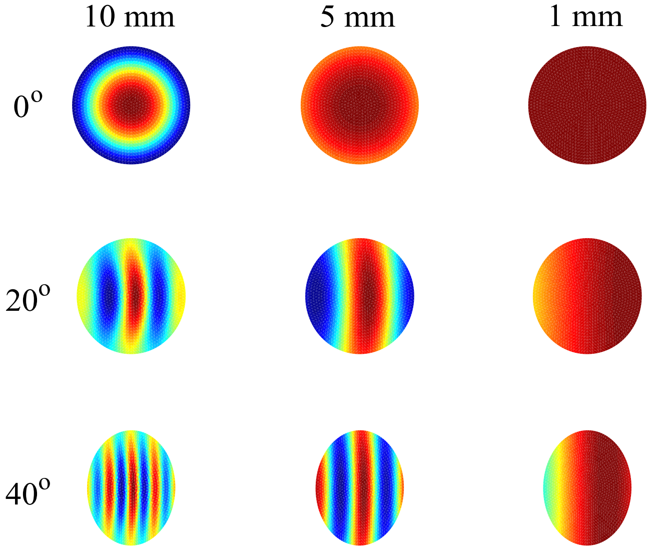

Figure 11. RX face pressure profiles for a 10 mm diameter TX operating at 939.6 kHz and a RX with 10, 5, and 1 mm diameter oriented at 0°, 20°, and 40°. The profiles are taken at 28.38 mm depth. Red represents high pressure and blue low pressure.

impedance is 5.367 MRayls in this case. It is observed that the reflection coefficient is about 0.52 for normal incidence and 1 at about 18.5° incident angle. It should be noted that not all of the pressures rays strike the RX at the same angle in realistic wave profiles as shown in figure 10. This means that the reflection coefficient must be considered in the aggregate of pressure rays to determine its total effect on voltage and power. Change 3, a change in RX face pressure profile can be observed in figure 11. As the RX is misoriented, vertical bands of high and low pressure appear on the RX face. The distance between these bands along the propagation axis is Δz, or half the wavelength in the medium. These bands appear in a similar fashion in the near-field and in the far-field. As the RX gets very close to the TX, the bands appear to be overlapped with a slight ripple because of high reflection activity that is able to occur. As the RX gets very far away from the TX, the bands are more sharply defined because of the lack of reflection activity. At 1 mm RX diameter in the figure, the bands do not make a significant appearance on the RX face because the RX diameter is on the same order as the band spacing, Δz.

$$R = \frac{\dfrac{Z_{\mathrm{RX}}}{\cos(\theta_t)} - \dfrac{Z_m}{\cos(\theta_i)}}{\dfrac{Z_{\mathrm{RX}}}{\cos(\theta_t)} + \dfrac{Z_m}{\cos(\theta_i)}}. \quad (2)$$

To compile the angle profiles that occur along the depth range of interest (10–50 mm), like those in figure 8, into a more broadly useful format: (1) voltage and power angle profiles are generated for fixed depths. The depths of most interest are the peaks and valleys of the depth profile. The voltage and power angle profiles at peaks and valleys from a 10 mm diameter TX and RX operating at 939.6 kHz are given in figure 12. These profiles are expressed as a percentage of the voltage and power at 0° angle, 0 mm offset, and the corresponding fixed depth. This means that at 0° angle, the voltage and power percentage is always 100%. In figure 12, the dark blue line represents the angle profile at a peak or valley nearest to 10 mm depth and the dark red line represents the angle profile at a peak or valley nearest to 50 mm depth. It is notable that the acoustic standing waves change the shape of the peak and valley angle profiles. (2) The angle at which each voltage or power angle profile intersects the half voltage or power line (dashed black line in figure 12) is measured and used to create the half angle design graph.

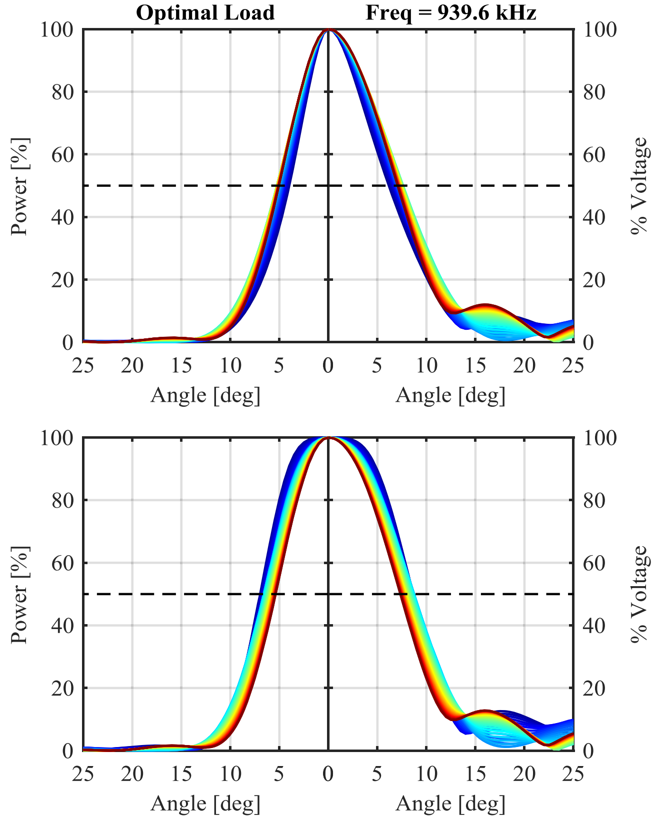

Figure 12. Angle profiles taken at peaks (top) and valleys (bottom) for a 10 mm diameter TX and RX operating at 939.6 kHz. Each line represents a fixed depth at a peak or valley from 10 mm (dark blue) to 50 mm (red). The angle at which each profile intersects the half voltage/power line is measured and used to create the half angle design graph.

The third design graph is the half angle design graph demonstrated in figure 13. This graph gives the angle at which the load voltage or power will be half of the load voltage or power seen at 0° angle. This angle is referred to as the half angle. In the figure, each line represents a RX diameter from 1 mm (dark blue) to 10 mm (red). An example of how to read this graph is as follows: at 45 mm depth, the half voltage angle of the red line (10 mm RX diameter) is about 7° and the half power angle is about 5°. This means that when the RX is at 45 mm depth, the load voltage will be reduced by half when the RX is misoriented by 7° and the power will be reduced by half when the RX is misoriented by 5°. The data in figure 13 show that the half angle is not a strong function of depth in the far-field and partially into the near-field (Rayleigh distance is 14.58 mm in the figure). However, the half

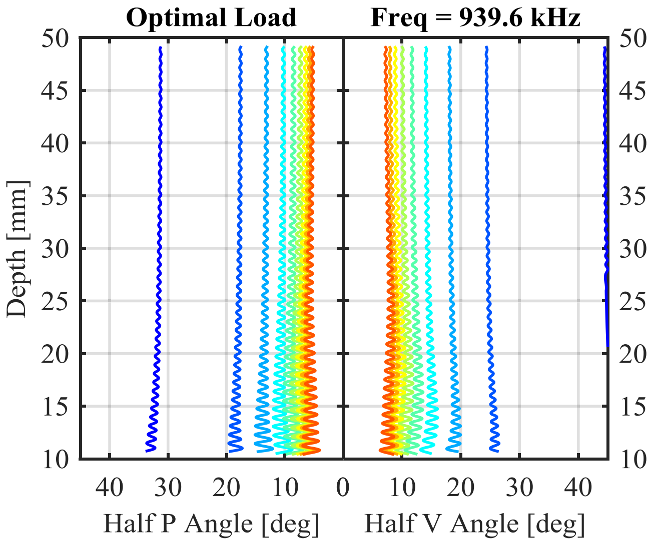

Figure 13. Half angle design graph for a 10 mm diameter TX operating at 939.6 kHz. Gives RX angle required to reduce the load voltage or power by half as a function of depth. Each line represents a RX diameter from 2 mm (dark blue) to 10 mm (red).

angle is a strong function of diameter. This is due to the band formation in the RX pressure profile as the RX is misoriented, as previously discussed. The oscillations in the half angle lines are due to acoustic standing waves and repeat at Δz intervals. These oscillations diminish as the RX gets farther away from the TX and as the acoustic impedance of the TX and RX approach the acoustic impedance of the medium.

Offset

The fourth parameter of interest is offset. Figure 14 is a depiction of TX and RX overlap as a function of offset. In the figure, the TX and RX are perfectly aligned when looking down the propagation axis at zero offset. When offset increases, as in the middle and right cases, the TX and RX become misaligned. Clearly, as they become misaligned, the RX will capture less of the transmitted power. Figure 15 gives voltage and power offset profiles for depths between a valley (at 13.78 mm depth) and a peak (at 14.22 mm depth) for a 10 mm diameter TX and RX operating at 939.6 kHz. In the figure, the peak (red) and valley (dark blue) lines converge to the same value (meaning no standing waves) as they approach 10 mm offset (offset at which there is no overlap between the TX and RX). To analyze the offset profiles from a broader point of view, normalized offset profiles are generated for each peak and valley between 10 and 50 mm depth in the same manner as described in the Angle section of this paper. A sample of these profiles for a 10 mm diameter TX and 3 mm diameter RX is given in figure 16. This figure is provided to clarify that when the RX diameter is smaller than the TX diameter and the RX is in the near-field, the voltage and power at zero offset and angle is not always the maximum value of the profile. This is due to the interference pattern in the near field that can have low intensity magnitudes near to the propagation axis and high intensity magnitudes offset

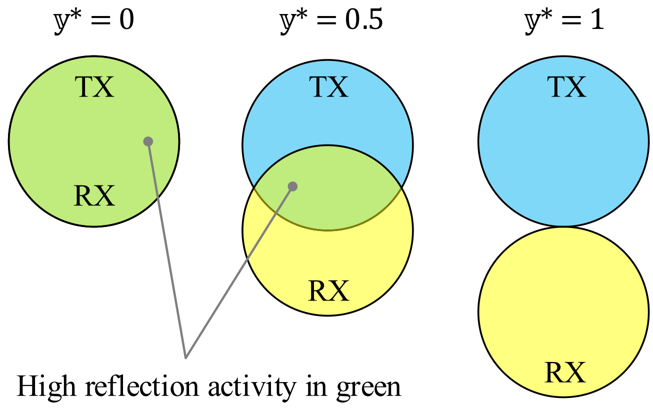

Figure 14. A depiction of TX and RX overlap as a function of alignment (offset). The blue area represents the TX, the yellow area represents the RX, and the green area represents the overlap of TX and RX when looking down the propagation axis. The green area additionally represents the region in which high reflection activity can occur.

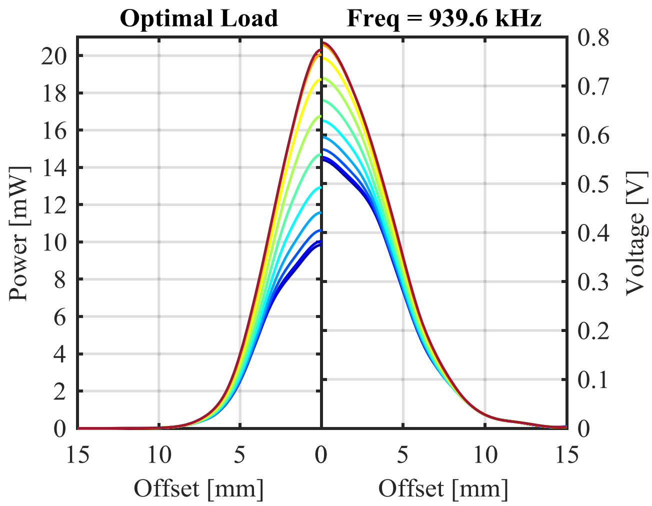

Figure 15. Voltage and power offset profile for a 10 mm diameter TX and RX operating at 939.6 kHz. Each line represents a fixed depth from 13.78 mm (dark blue) to 14.22 mm (red). The 13.78 mm line represents a valley and the 14.22 mm line represents a peak.

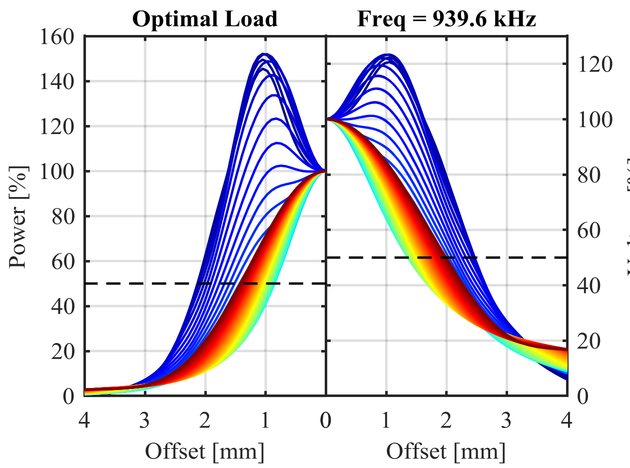

Figure 16. Offset profiles taken at peaks for a 10 mm diameter TX and 3 mm diameter RX operating at 939.6 kHz. Each line represents a fixed depth at a peak from 10 mm (dark blue) to 50 mm (red).

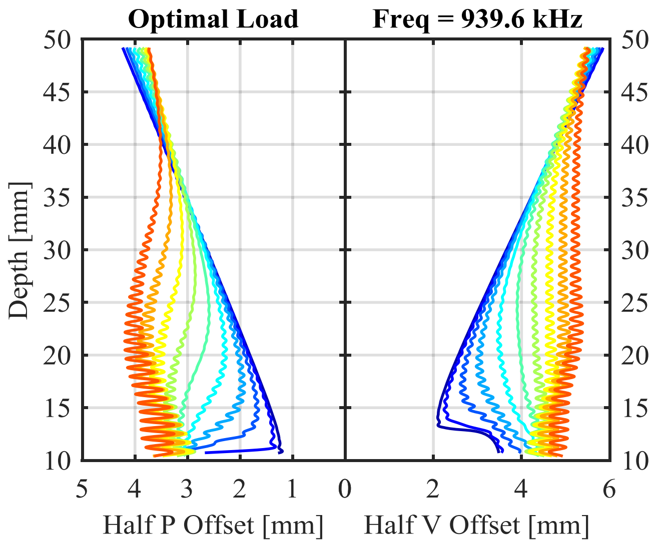

Figure 17. Half offset design graph for a 10 mm diameter TX operating at 939.6 kHz. Gives RX offset required to reduce the load voltage or power by half as a function of depth. Each line represents a RX diameter from 1 mm (dark blue) to 10 mm (red).

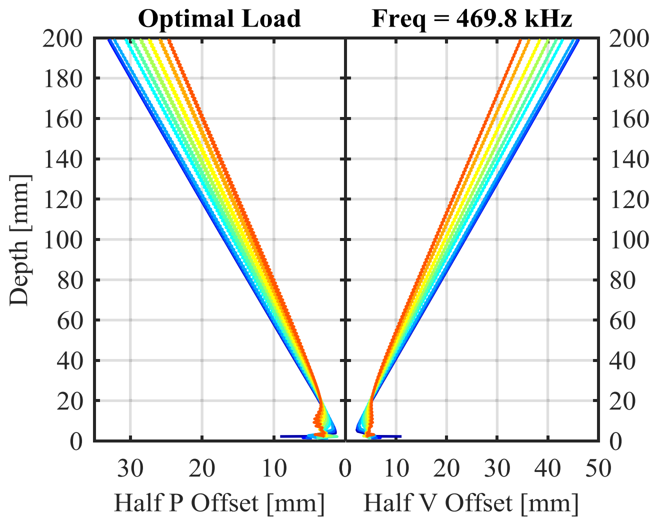

Figure 18. Extended half offset design graph at 469.8 kHz. Each line represents a RX diameter from 1 mm (dark blue) to 10 mm (red).

from the propagation axis as shown in figure 6 at about 0.2, 2.3, and 7 mm depths. Nevertheless, the half voltage and power lines are still calculated as being half of the value at zero offset and zero angle. The offset at the intersection of these lines and the offset profile is measured and compiled into the half offset design graph.

The fourth design graph is the half offset design graph demonstrated in figure 17. The half offset design graph gives the offset at which the load voltage or power will be reduced to half of the load voltage or power seen at zero offset. This offset is referred to as the half offset. In the figure, each line represents a RX diameter from 1 mm (dark blue) to 10 mm (red). An example of how to read this graph is as follows: at 20 mm depth, the half voltage offset of the green line (6 mm RX diameter) is about 4 mm and the half power offset is about 2.7 mm. This means that when the RX is at 20 mm depth, the load voltage will be reduced by half when the RX is misaligned by 4 mm and the load power will be reduced by half when the RX is misaligned by 2.7 mm. The half offset dark blue line, in figure 17, appears to be diverging from the propagation axis at a nearly constant angle. This divergence angle can be approximated in the far-field for RX diameters that are small relative to the TX diameter by calculating the directivity of the acoustic beam as given in (3) [30], where H is the directivity of the acoustic beam emitted from the TX, k is the wave number, a is the radius of the TX and ϕ is the angle relative to the propagation axis. In the half voltage offset graph, the divergence angle is calculated by setting H equal to 0.5 and solving for ϕ. In the half power offset graph, the divergence angle is calculated by setting H^2 equal to 0.5 and solving for ϕ. A comparison of calculated divergence angles and measured divergence angles from 6 sets of half voltage and power offset graphs yields a mean 4.2% error with 1.32% standard deviation. The measurements from simulation data were taken using a 1 mm diameter RX, 10 mm diameter TX, and frequencies from 600 to 1350 kHz in increments of 150 kHz. All of the measured angles were smaller than the calculated divergence angles. When approximating or measuring the divergence angle, it should be noted that the line of the divergence angle does not pass through the center of the TX face. For RX diameters that are of similar size to the TX, a divergence angle does occur but takes longer to form and is smaller than the calculated divergence angle as shown in the extended half offset design graph in figure 18. In the figure, it is notable that the data trends appear slightly different than in figure 17. This is due to differences in the Rayleigh distance. In figure 17 the Rayleigh distance is 14.58 mm while it is 6.67 mm in figure 18. It is important to note that the data trends in figure 17 are actually similar to the data trends to figure 18 (when looking at a larger depth range) but are effectively stretched by a factor $14.58/6.67 = 2.19$ in the depth direction such that the shape of the data in figure 17 between 10 and 50 mm depth appears in figure 18 between 4.5 and 22.8 mm depth.

$$\mathrm{H} = \frac{2J_1(ka\,\sin(\phi))}{ka\,\sin(\phi)}. \tag{3}$$

It is important to note that the effects of angle misorientation and offset misalignment do not linearly superimpose. When the RX is offset from the propagation axis, the intensity seen on the RX face is no longer axially symmetric. For example, the power delivered to the load for a 10 mm TX and RX operating at 469.8 kHz and 20 mm depth experiences a 40.7% reduction for a 3 mm offset and a 16.6% reduction for a 5° angle separately. At a combined 3 mm offset and +5° angle, the power is reduced by 32.5%. At a combined 3 mm offset and −5° angle, the power is reduced by 63.5%. Neither of these percentages correspond to the superposition combined reduction of 49.5%.

Table 3. Assignment of variables to system parameters with accompanying non-dimensional expressions.

Parameter	Variable	Non-dimensional expression
TX diameter	D_{TX}	$D^*_{\mathrm{TX}} = D_{\mathrm{TX}}/D_{\mathrm{TX}} = 1$
RX diameter	D_{RX}	$D^*_{\mathrm{RX}} = D_{\mathrm{RX}}/D_{\mathrm{TX}}$
Depth	z	$z^* = z/D_{\mathrm{TX}}$
Angle	θ_X	θ_X
Offset	y	$y^* = y/D_{\mathrm{TX}}$
Frequency	f	$f^* = D_{\mathrm{TX}}/\lambda = fD_{\mathrm{TX}}/c$
Load impedance	R_L	$R^*_L = R_L/R_{L,\mathrm{opt,avg}}$
RMS voltage	V	$V^* = V/D_{\mathrm{TX}}$
Avg. power	P	$P^* = P/D^2_{\mathrm{TX}}$

Non-dimensional analysis

To apply the four design graphs developed in this paper to a wider range of dimensional system parameters, non-dimensional parameters and design graphs are presented in this section. Table 3 provides a reference of non-dimensional expressions for system parameters. The variables used are consistent with the variables in [27] and are summarized as follows: z is the depth or axial separation distance between the TX and RX, θ_X is the angle between the TX and RX faces, y is the offset or lateral offset distance between the TX and RX, D_{TX} is the diameter of the TX, D_{RX} is the diameter of the RX, f is the operating frequency of the TX, c is the speed of sound in the medium, λ is the acoustic wavelength in the medium, R_L is the impedance of the load, $R_{L,\mathrm{opt,avg}}$ is the fixed-average optimal load resistance, V is the RMS voltage measured across the RX load, and P is the average power delivered to the RX load. The non-dimensional expressions given in table 3. are defined as follows: all length dimensions in the system are non-dimensionalized with respect to the TX diameter and the RX load is non-dimensionalized with respect to the fixed-average optimal load impedance. The TX diameter is chosen as the non-dimensional length parameter because its value, along with wavelength, determine the emitted acoustic beam pattern. The beam pattern, in turn, determines the sensitivity of voltage and power to depth, angle, and offset.

The four types of design graphs previously explained are generated using the sweep range of non-dimensional parameters given in table 4. The table additionally provides the dimensional parameters used to create the non-dimensional graphs. Even though dimensional parameters are used to create the design graphs, the data hold for any actual dimensions. The non-dimensional set of design graphs can be converted to dimensional units by using the relationships found in table 3 and the correction factors discussed later in this section. The design graphs should be regenerated if assuming different piezoelectric properties, transducer layers, layer thickness ratios, or medium properties than assumed in this paper. The thickness ratio of the transducers assumed in this paper are 0.45. This means that the piezo layer is 45% of the total transducer thickness (piezo layer plus titanium layer). The non-dimensional design graphs that follow provide additional insights about the effect that frequency plays in voltage and power.

Table 4. Parameter sweep values considered in this paper given in non-dimensional parameters (top half). Actual dimensional values used to generate design graphs (bottom half).

Parameter	Var	Units	Min	Incr	Max
Depth*	z^*	—	1	$1/30f^*$	5
Offset*	y^*	—	0	0.015	1.5
RX diameter*	D^*_{RX}	—	0.1	0.1	1
Frequency*	f^*	—	3	3	9
Load*	R^*_L	—	1	1	1
Depth	z	mm	10	$c/(30f)$	50
Angle	θ_X	deg	0	0.5	45
Offset	y	mm	0	0.15	15
TX diameter	D_{TX}	mm	10	—	10
RX diameter	D_{RX}	mm	1	1	10
Frequency	f	kHz	469.8	469.8	1409.4

The non-dimensional depth magnitude design graphs are given in figure 19. Each of the figures represents a different frequency (a higher value of f^* means a higher frequency) and all figures assume optimal load. The lines in each of the graphs correspond to a non-dimensional RX diameter, D^*_{RX}, from 0.1 (dark blue) to 1 (red). A non-dimensional RX diameter of 0.1 means that the dimensional RX diameter is 10% of the TX diameter. In the figures, it is observed that an increase in frequency has the general effect of decreasing both power and voltage. This is due to the high absorption coefficient of the assumed medium properties. A general effect of increased frequency in the design graphs is the increase in the Rayleigh distance. As previously discussed, a change in Rayleigh distance has the effect of stretching the data trends in the depth direction as frequency is increased. Before extracting data from the depth magnitude design graph, it is important to note that the final average power dimensional value must be multiplied by a scaling correction factor as given in figure 20. The correction factor is numerically generated by compiling data from multiple scaled design graphs into a correction band that is valid for all values in the depth magnitude design graphs. The correction factor does not need to be applied to the final dimensional RMS voltage because its correction factor is approximately one for all TX diameters. An example of how to extract dimensional values from the non-dimensional depth magnitude design graphs is as follows: a 12.7 mm diameter TX and 6.35 mm diameter RX operating at 1110 kHz are placed 20 mm apart. RX Diameter* (D^*_{RX}) is calculated as $12.7/6.35 = 0.5$ which corresponds to the cyan lines. Frequency* (f^*) is calculated as $1110\,000 * 0.0127/1566 = 9.00$ which corresponds to the bottom graph. Depth* (z^*) is calculated as $20/12.7 = 1.57$. The correction factor from figure 20 for a 12.7 mm diameter TX is found to be about 1.07. The depth magnitude design graph in figure 19 (bottom graph, cyan line) gives about 54 for RMS Voltage* (V^*) and about 46 for Avg. Power* (P^*). In dimensional form, this gives the mean magnitude as $54 * 0.0127 = 0.686$ V_{RMS} and $46 * 0.0127\hat{}2 * 1.07 = 0.007\,94$ W $= 7.94$ mW for 7200 W m^{-2} intensity emitted

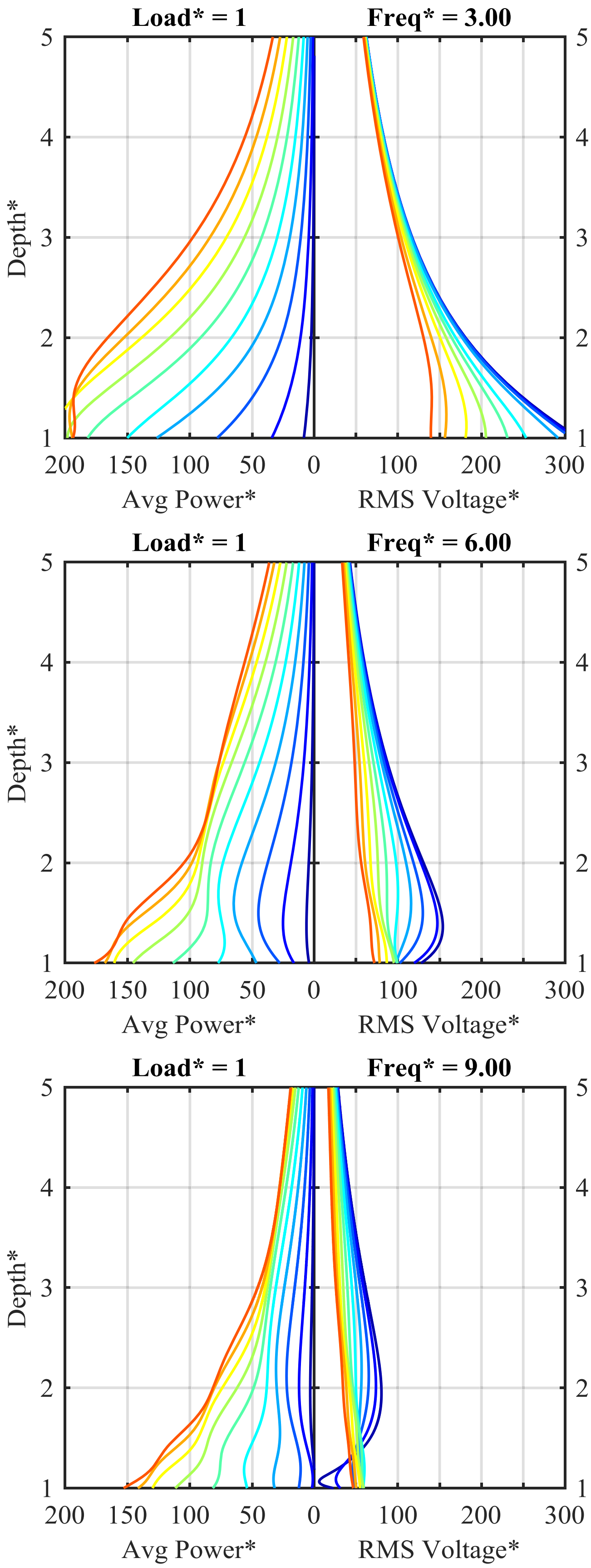

Figure 19. Non-dimensional depth magnitude design graphs. Each line represents D_{RX}^{*} from 0.1 (dark blue) to 1 (red).

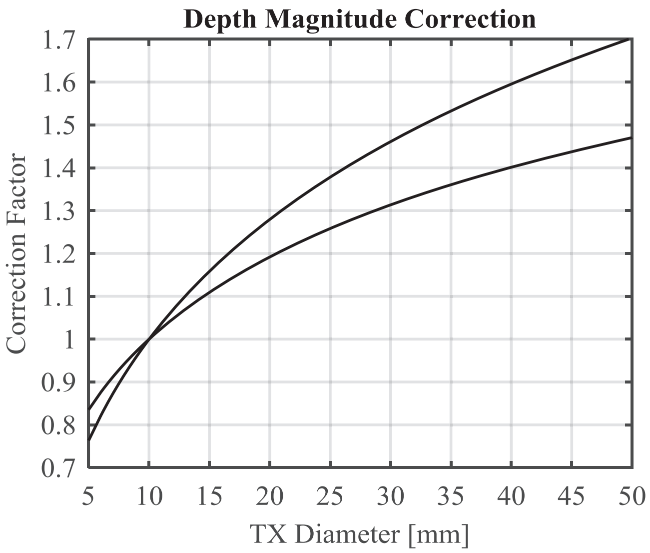

Figure 20. Correction factor for non-dimensional depth magnitude design graph. The two lines represent the upper and lower limits of correction certainty.

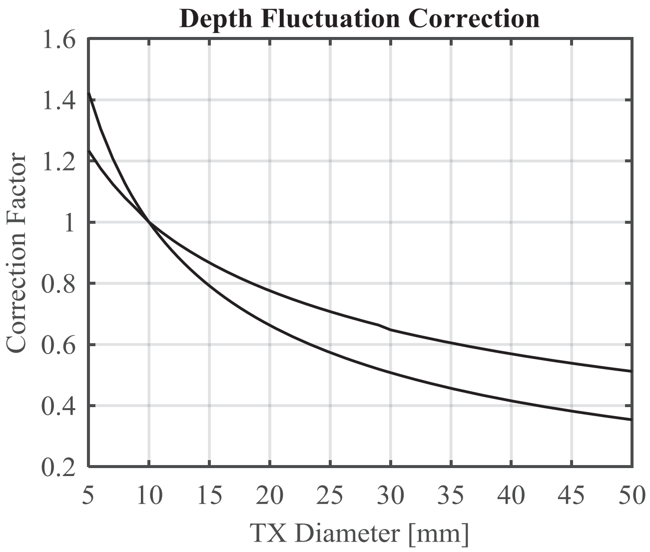

Figure 21. Correction factor for non-dimensional depth fluctuation design graph. The two lines represent the upper and lower limits of correction certainty.

from the TX face. To put this in terms of efficiency, $7200 * \pi * 0.0127\hat{}2/4 = 91.2$ mW is emitted into the medium by the TX which means that the system efficiency is $7.86/91.2 = 8.7\%$.

The non-dimensional depth fluctuation design graphs are given in figure 22. Upon close inspection, these graphs are also subject to Rayleigh distance stretching and medium absorption. When converting depth fluctuation design graph data to dimensional units, a correction factor is first obtained from figure 21 based on the TX diameter. From the figure, the correction factor for a 12.7 mm diameter RX is found to be about 0.9. Unlike the depth magnitude correction factor, the depth fluctuation correction factor must be applied to voltage and

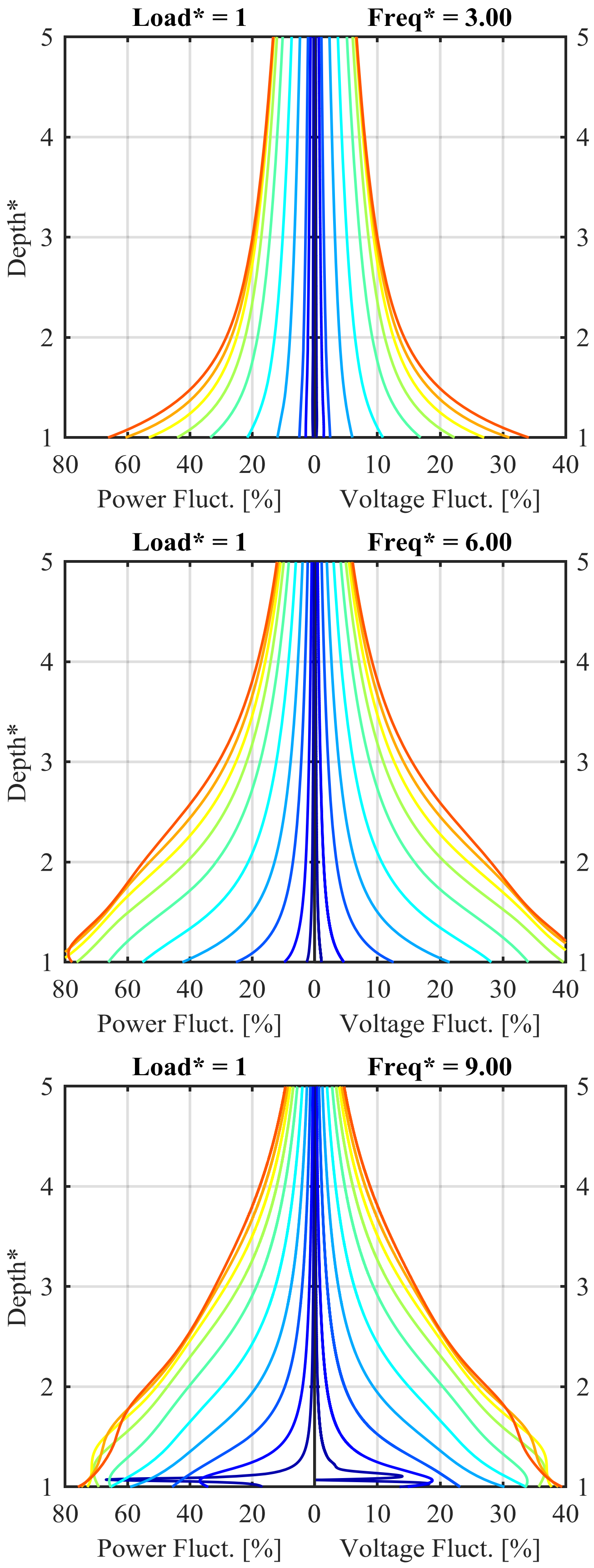

Figure 22. Non-dimensional depth fluctuation design graphs. Each line represents D^{*}_{RX} from 0.1 (dark blue) to 1 (red).

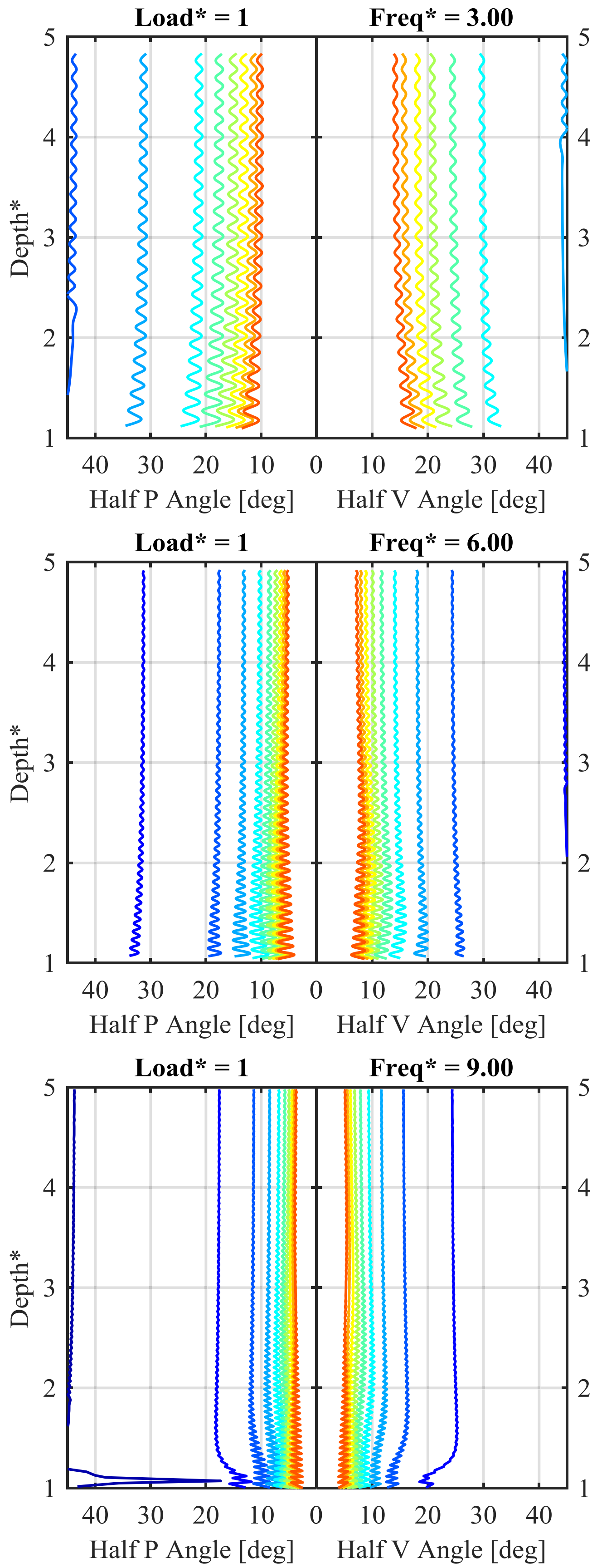

Figure 23. Non-dimensional half angle design graphs. Each line represents D^{*}_{RX} from 0.1 (dark blue) to 1 (red).

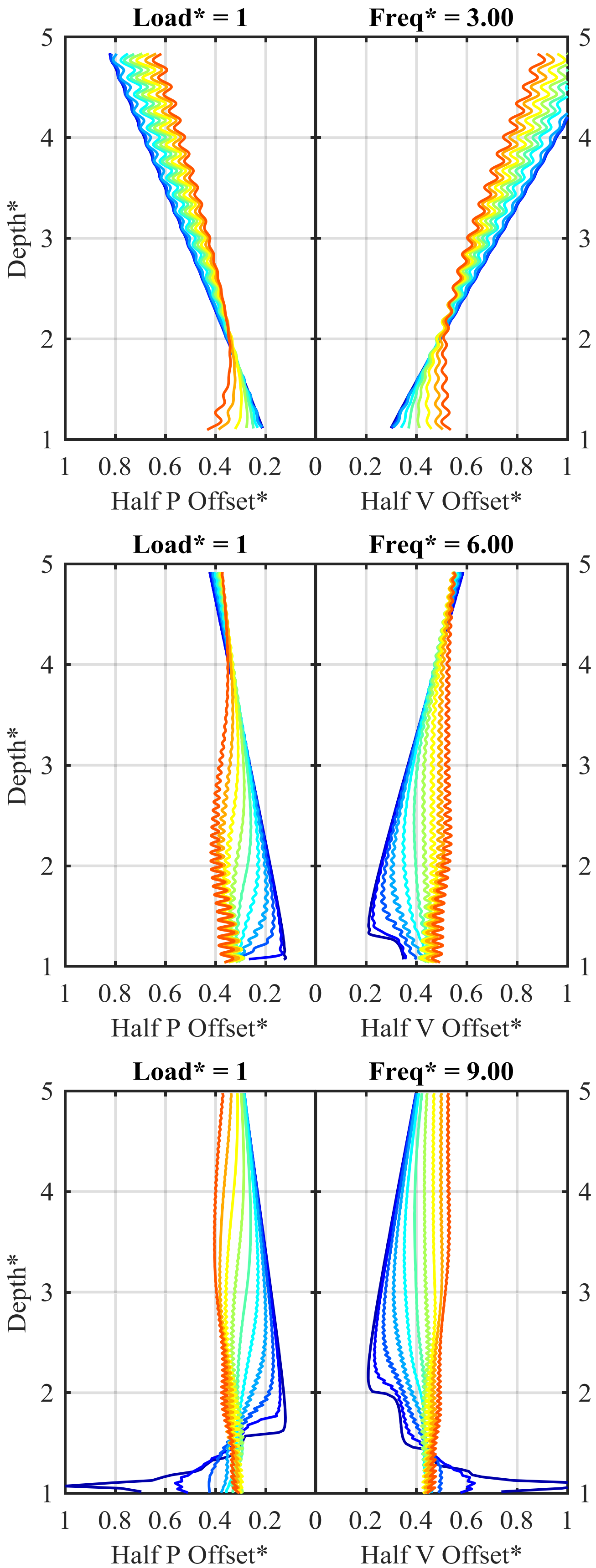

Figure 24. Non-dimensional half offset design graphs. Each line represents D^{*}_{RX} from 0.1 (dark blue) to 1 (red).

power fluctuation dimensional values. Continuing the example from the previous paragraph, the bottom graph and cyan lines are consulted. The corresponding voltage fluctuation is about 21% and the power fluctuation is about 42%. As an intermediate step, the half wavelength in the medium (Δz) is calculated as $1566/1110\,000/2 = 0.705$ mm. Converting to dimensional form, the RX experiences a maximum voltage fluctuation of $0.21 * 0.686 * 0.9 = 0.13$ V_{RMS} and a power fluctuation of $0.42 * 7.86 * 0.9 = 2.97$ mW when its position is disturbed in the depth direction by as little as $0.705/2 = 0.353$ mm to $3 * 0.705/4 = 0.529$ mm.

The non-dimensional half angle design graphs are given in figure 23. The half angle is observed to be a strong function of frequency. As discussed in the Angle section of this paper and illustrated in figure 11, pressure bands form on the RX face as angle increases. The spacing of the bands is Δz in the depth direction, which is a function of frequency. As frequency increases, the bands appear at smaller RX angles, thus increasing the sensitivity of voltage and power to disturbances in RX angle. It should be noted that unlike the depth magnitude and depth fluctuation design graphs, the half angle design graph does not require a correction factor. However, the amplitude of the oscillations in the half angle lines increases/decreases with an increase/decrease in voltage and power fluctuation percent. Continuing the example from the previous paragraphs, the bottom graph and cyan lines are consulted. The corresponding half voltage angle is about 8.9° and the half power angle is about 6.3°. This means that the load voltage is reduced to $0.686/2 = 0.343$ V_{RMS} at an 8.9° disturbance in RX orientation, and the power is reduced to $7.86/2 = 3.93$ mW at a 6.3° disturbance.

The non-dimensional half offset design graphs are given in figure 24. The half offset is a strong function of frequency. Higher frequencies result in a narrower beam, which decreases the divergence angle of the half offset lines as discussed in the Offset section of this paper. This means that voltage and power are more sensitive to disturbances in offset at higher frequencies. Another way of considering this effect is to observe that higher frequencies increase the Rayleigh distance, which effectively stretches the half offset line trends in the depth direction. The half offset design graphs, like the half angle design graphs, do not require a correction factor and the amplitude of the half offset line oscillations increases with an increase in voltage and power fluctuation. Continuing the example from the previous paragraphs, the bottom graph and cyan lines are once again consulted. The corresponding half voltage offset is about 0.43 and the half power offset is about 0.315. This means that the load voltage is reduced to $0.686/2 = 0.343$ V_{RMS} at a $0.43 * 12.7 = 5.46$ mm disturbance in RX alignment, and the power is reduced to $7.86/2 = 3.93$ mW at a $0.315 * 12.7 = 4$ mm disturbance.

Conclusion

This paper provided an analysis of load voltage and power magnitude and sensitivity to disturbances in RX depth, orientation, and alignment for acoustic power transfer systems. The dependence of voltage and power on load, diameter, and operating frequency was also explored. Four types of design graphs were developed: depth magnitude, depth fluctuation, half angle, and half offset. The depth magnitude design graph provides details about the mean voltage and power as a function of depth. The depth fluctuation design graph provides the maximum change in voltage and power the load will experience for a depth disturbance of at least $\Delta z/2$ to $3\Delta z/2$. The half angle and offset graphs provide the angle and offset at which the voltage and power will be reduced to half of its zero-angle-zero-offset value. Non-dimensional analysis and graphs were then provided to extend applicability to a wider range of scenarios. Correction factors were introduced to allow proper scaling of the non-dimensional depth magnitude and fluctuation graphs. These graphs can be thought of as providing information to system designers on the range of uncertainty in voltage and power that their system may see as a result of uncertainty in RX location and orientation.

Funding

The authors gratefully acknowledge funding from the National Science Foundation under grant number ECCS-1408265.

ORCID iDs

David B Christensen https://orcid.org/0000-0003-1488-1534

References

[1] Basaeri H, Christensen D B and Roundy S 2016 A review of acoustic power transfer for bio-medical implants *Smart Mater. Struct.* **25** 1–23
[2] Kawanabe H, Katane T, Saotome H, Saito O and Kobayashi K 2001 Power and Information transmission to implanted medical device using ultrasonic *Japan. J. Appl. Phys.* **40** 3865–6
[3] Suzuki S-N, Kimura S, Katane T, Saotome H, Saito O and Kobayashi K 2002 Power and interactive information transmission to implanted medical device using ultrasonic *Japan. J. Appl. Phys.* 1 **41** 3600–3
[4] Arra S, Leskinen J, Heikkilä J and Vanhala J 2007 Ultrasonic power and data link for wireless implantable applications *Int. Symp. on Wireless Pervasive Computing* pp 567–71
[5] Ozeri S and Shmilovitz D 2010 Ultrasonic transcutaneous energy transfer for powering implanted devices *Ultrasonics* **50** 556–66
[6] Denisov A and Yeatman E 2010 Ultrasonic versus inductive power delivery for miniature biomedical implants *2010 Int. Conf. on Body Sensor Networks BSN* pp 84–9
[7] Shigeta Y, Hori Y, Fujimori K, Tsuruta K and Nogi S 2011 Development of highly efficient transducer for wireless power transmission system by ultrasonic *2011 IEEE MTT-S Int. Microwave Workshop Series on Innovative Wireless Power Transmission: Technologies, Systems, and Applications* pp 171–4
[8] Ozeri S, Spivak B and Shmilovitz D 2012 Non-invasive sensing of the electrical energy harvested by medical implants powered by an ultrasonic transcutaneous energy transfer link *IEEE Int. Symp. Industrial Electronics* pp 1153–7
[9] Sanni A, Vilches A and Toumazou C 2012 Inductive and ultrasonic multi-tier interface for low-power, deeply implantable medical devices. *IEEE Trans. Biomed. Circuits Syst.* **6** 297–308
[10] Hori Y, Fujimori K, Tsuruta K and Nogi S 2012 Design and development of highly efficient transducer for ultrasonic wireless power transmission system *IEEJ Trans. Electron. Inf. Syst.* **132** 337–43
[11] Lee S Q, Youm W and Hwang G 2013 Biocompatible wireless power transferring based on ultrasonic resonance devices *Proc. Meetings Acoustics* vol 19, pp 1–9
[12] Mo C, Hudson S and Radziemski L J 2013 Effect of misalignment between ultrasound piezoelectric transducers on transcutaneous energy transfer **8688** 868814
[13] Seo D, Carmena J M, Rabaey J M, Alon E and Maharbiz M M 2013 Neural dust: an ultrasonic, low power solution for chronic brain-machine arXiv:1307.2196
[14] Shahab S and Erturk A 2014 Contactless ultrasonic energy transfer for wireless systems: acoustic-piezoelectric structure interaction modeling and performance enhancement *Smart Mater. Struct.* **23** 125032
[15] He Q, Liu J, Yang B, Wang X, Chen X and Yang C 2014 MEMS-based ultrasonic transducer as the receiver for wireless power supply of the implantable microdevices *Sensors Actuators* A **219** 65–72
[16] Lee S Q, Youm W, Hwang G, Moon K S and Ozturk Y 2014 Resonant ultrasonic wireless power transmission for bio-implants **9057** 90570J
[17] Ozeri S and Shmilovitz D 2014 Simultaneous backward data transmission and power harvesting in an ultrasonic transcutaneous energy transfer link employing acoustically dependent electric impedance modulation *Ultrasonics* **54** 1929–37
[18] Chou T C, Subramanian R, Park J and Mercier P P 2014 A miniaturized ultrasonic power delivery system *IEEE 2014 Biomed. Circuits Systems Conf. BioCAS 2014—Proc.* pp 440–3
[19] Vihvelin H, Leadbetter J, Bance M, Brown J A and Adamson R B A 2015 Compensating for tissue changes in an ultrasonic power link for implanted medical devices *IEEE Trans. Biomed. Circuits Syst.* (https://doi.org/10.1109/TBCAS.2015.2421823)
[20] Christensen D B and Roundy S 2015 Ultrasonically powered piezoelectric generators for bio-implantable sensors: plate versus diaphragm *J. Intell. Mater. Syst. Struct.* **27** 1–14
[21] Song S H, Kim A and Ziaie B 2015 Omni-directional ultrasonic powering for mm-scale implantable biomedical devices *IEEE Trans. Biomed. Eng.* **62** 2717–23
[22] Zhou J, Kim A and Ziaie B 2015 An ultrasonically controlled power management system for implantable biomedical devices *Biomedical Circuits Systems* pp 1–4
[23] Fang B, Feng T, Zhang M and Chakrabartty S 2015 Feasibility of B-mode diagnostic ultrasonic energy transfer and telemetry to a cm2 sized deep-tissue implant *Proc.—IEEE Int. Symp. Circuits Systems* vol 2015, pp 782–5
[24] Charthad J, Weber M J, Chang T C and Arbabian A 2015 A mm-sized implantable medical device (IMD) with ultrasonic power transfer and a hybrid bi-directional data link *IEEE J. Solid-State Circuits* **50** 1741–53
[25] Radziemski L and Makin I R S 2016 *In vivo* demonstration of ultrasound power delivery to charge implanted medical

devices via acute and survival porcine studies *Ultrasonics* **64** 1–9
[26] Shmilovitz D, Ozeri S, Wang C C and Spivak B 2014 Noninvasive control of the power transferred to an implanted device by an ultrasonic transcutaneous energy transfer link *IEEE Trans. Biomed. Eng.* **61** 995–1004
[27] Christensen D B, Basaeri H and Roundy S 2017 A computationally efficient technique to model depth, orientation and alignment via ray tracing in acoustic power transfer systems *Smart Mater. Struct.* **26** 125020
[28] Schmerr L 2015 *Fundamentals of Ultrasonic Phased Arrays* (Cham: Springer) (https://doi.org/10.1007/978-3-319-07272-2)
[29] Kinsler L, Frey A, Coppens A and Sanders J 1999 *Fundamentals of Acoustics* 4th edn (New York: Wiley)
[30] Christensen D A 1988 *Ultrasonic Bioinstrumentation* (New York: Wiley)
[31] U.S. Department of Health and Human Services, Food and Drug Administration, Center for Devices and Radiological Health 2008 Guidance for Industry and FDA Staff Information for Manufacturers Seeking Marketing Clearance of Diagnostic Ultrasound Systems and Transducers
[32] McGough R J, Samulski T V and Kelly J F 2004 An efficient grid sectoring method for calculations of the near-field pressure generated by a circular piston *J. Acoust. Soc. Am.* **115** 1942–54